

In-Phase Bias Modulation Mode of Scanning Ion Conductance Microscopy With Capacitance Compensation

Peng Li, *Student Member, IEEE*, Lianqing Liu, *Member, IEEE*, Yang Yang, Yuechao Wang, *Member, IEEE*, and Guangyong Li, *Member, IEEE*

Abstract—The in-phase bias modulation (IPBM) mode of scanning ion conductance microscopy (SICM), which has advantages of both the dc mode and the traditional ac mode, is immune to low-frequency external electronic interference and potential drift while maintaining a high scanning speed. However, the IPBM mode still suffers from a low-signal-to-noise ratio (SNR). In this paper, we propose a capacitance compensation (CC) method to solve the problem in the IPBM mode of SICM. After CC, the signal level is significantly increased while the noise level remains unchanged. The increased SNR not only improves the image quality but also allows the system to work at a higher modulation frequency, thus increasing potential for fast scan. Experimental results verify the effectiveness of the IPBM mode of SICM with CC.

Index Terms—Capacitance compensation (CC), in-phase bias modulation (IPBM) mode, scanning ion conductance microscopy (SICM), signal-to-noise ratio (SNR).

I. INTRODUCTION

SCANNING ion conductance microscopy (SICM), which was introduced in 1989 [1], is a nanoscale imaging technology that is based on the use of a nanopipette tip that scans the area above a sample. By monitoring the ion current flowing through the nanopipette to maintain the tip-sample separation at a distance approximately equal to the inner radius of the tip, SICM applies a negligible force on the sample. Thus, SICM can provide precise height measurements for soft materials on

nanoscale level [2]. Because of its noninvasive, high-resolution, and non-force contact imaging characteristics, SICM has become a promising tool in different fields. In biology [3], it is used for noninvasive imaging [4], nano-injection [5], single-cell nanobiopsy [6], noncontact mechanical stimulation [7], and smart patch clamp [8]. In electrochemistry, it is used for simultaneous topographical and electrochemical detection [9], [10] and mapping the surface activity of individual nanoparticles [11], whereas in physics, it is used to provide a novel light source for scanning near-field optical microscopy [12].

There are several main scanning modes that are used to regulate the tip-sample distance in SICM. The simplest one is dc mode [13], in which the current induced by a fixed dc bias voltage is directly used as the feedback during scanning. However, the dc mode is rarely used in practice because of its current instability (dc drift), which is attributed to either slowly developing dc potentials at the electrode tip or temperature fluctuations. To address the problem of dc drift, the ac mode was introduced [14], [15], which is a more reliable and robust control mode. Similar to the tapping mode of atomic force microscopy (AFM) [16], [17], in the ac mode, either the tip or the stage vibrates at a modulation frequency f in the z -axis direction, producing an induced ac current at the same modulation frequency f when the tip is close to the sample. The induced ac current is then used to control the tip-sample separation. However, the modulation frequency in the ac mode is limited by the response bandwidth of the piezoactuator and is usually within the range of 1 kHz to several kilohertz [14], [15]. This low modulation frequency limits the bandwidth of the overall feedback loop, therefore reducing the scanning speed [18] (please refer to Appendix I for further details). The Besenbacher group reported that imaging the same sample using SICM in ac mode at a modulation frequency of 1 kHz is five times slower than using conventional AFM in tapping mode at 34 kHz [2]. Another well-known SICM imaging mode is the hopping mode [4] and its variants [19]–[22]. By functioning as conducting an approach curve at every point, the hopping mode and its variants are able to image steep obstacles without collisions and are therefore suitable for imaging complex samples. However, the hopping mode is considerably slow because of the point-by-point approach.

Recently, two similar SICM imaging modes have been independently introduced by two research groups, namely, the bias-modulated (BM) mode [23], which was proposed by the

Manuscript received September 28, 2014; revised January 4, 2015 and February 11, 2015; accepted March 10, 2015. Date of publication March 30, 2015; date of current version September 9, 2015. This work was supported in part by the National Natural Science Foundation of China under Project 61433017 and Project 61327014, in part by the Instrument Development Project of the Chinese Academy of Sciences (CAS) under Project YZ201245, and in part by the CAS FEA International Partnership Program for Creative Research Teams.

P. Li is with the State Key Laboratory of Robotics, Shenyang Institute of Automation, Chinese Academy of Sciences, Shenyang 110016, China, and also with the University of the Chinese Academy of Sciences, Beijing 100049, China.

L. Liu, Y. Yang, and Y. Wang are with the State Key Laboratory of Robotics, Shenyang Institute of Automation, Chinese Academy of Sciences, Shenyang 110016, China (e-mail: lqliu@sia.cn).

G. Li is with the Department of Electrical and Computer Engineering, University of Pittsburgh, Pittsburgh, PA 15213 USA (e-mail: gli@engr.pitt.edu).

Color versions of one or more of the figures in this paper are available online at <http://ieeexplore.ieee.org>.

Digital Object Identifier 10.1109/TIE.2015.2417126

Unwin group, and the in-phase bias modulation (IPBM) mode [24], which was proposed by our group. In both of these modes, instead of vibrating the tip or the stage, an ac current is induced by an alternative voltage applied between the electrodes. The induced ac current is then used as the feedback to regulate the tip–sample separation during scanning. These two modes not only have the advantages of the traditional ac mode, including being free of dc drift and immune to low-frequency external electrical interference, but also possess the benefits of the dc mode, including high scanning speed and the absence of mechanical oscillation. In BM-SICM, either the amplitude or the phase component of the ac current is used for feedback. However, the sensitivity of the amplitude or the phase to the tip–sample separation significantly decreases with an increase in the modulation frequency; thus, it may not work at a relatively high frequency (i.e., over 10 kHz). In IPBM-SICM, only the part of the ac current that is in phase with the applied ac voltage is used for feedback. Our experiments show that IPBM-SICM can work stably at a higher modulation frequency (more than 10 kHz) and can therefore realize a faster scanning speed [24].

Although the IPBM mode has a good potential for the development of high-speed SICM, the modulation frequency is still limited by the low-signal-to-noise ratio (SNR) in the IPBM mode. Because of the capacitance effect in the circuit, the ratio of the in-phase part of the ac current to the total ac current becomes increasingly smaller as the frequency continues to increase. However, a further increase in the amplitude of the applied voltage will not solve the problem as the maximum allowable amplitude of the induced ac current is limited by the input range of the lock-in amplifier.

In this paper, we propose a capacitance compensation (CC) method to solve the low-SNR problem in IPBM-SICM. The CC method significantly increases the signal level while the noise level remains unchanged. The increased SNR not only significantly improves the image quality but also allows the system to work at a higher modulation frequency and, thus, a higher scanning speed. In our system, a maximum modulation frequency of 25 kHz, which is comparable with the typical tapping frequencies in AFM, has been tested for the IPBM mode that is enabled by the CC method, which yields a satisfactory performance. As a result, the IPBM-SICM with CC is expected to have a similar scanning speed as that obtained by AFM in tapping mode. We performed experiments on scanning over polydimethylsiloxane (PDMS) samples to verify the advantages of this method.

II. INTRODUCTION TO IPBM-SICM

The schematic of our IPBM-SICM system was reported in our previous work [24] and is illustrated in Fig. 1. In IPBM-SICM, a sinusoidal voltage signal $10U_{ac}$, with frequency f , is generated by a function generator and then attenuated by ten times through a patch clamp amplifier. The voltage signal is then applied across the two electrodes, i.e., one inside the nanopipette and the other in the solution. An ac current is induced by the ac voltage, which is amplified by the I – V converter in the patch clamp amplifier. The amplified ac current signal (in units of voltage) is then sent to a lock-in amplifier.

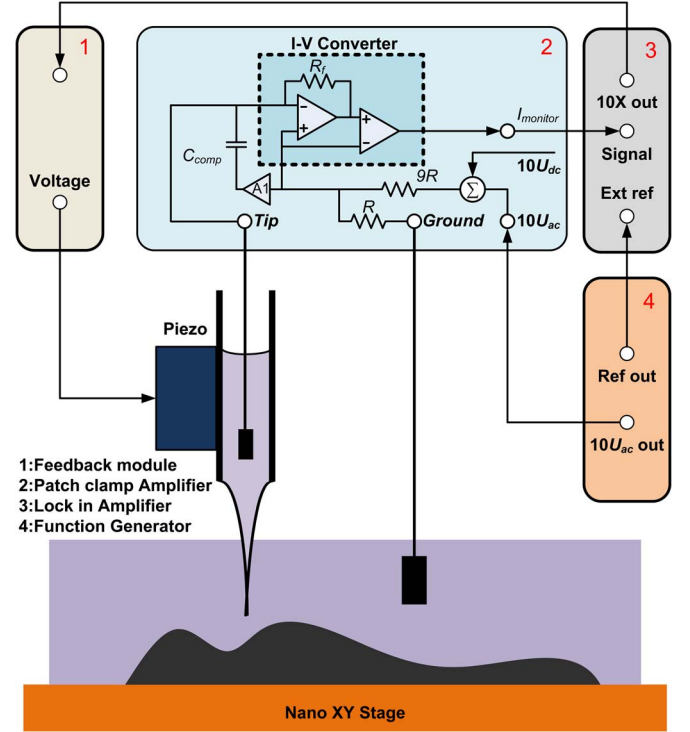


Fig. 1. Schematic of SICM in the IPBM mode.

The lock-in amplifier detects the portion of the amplified ac current that is locked at frequency f and then splits the portion into two parts. The part that is in phase with the driving sinusoidal voltage (the ten times X-output of the lock-in amplifier; please refer to Appendix II) is amplified tenfold and used as a feedback input to control the tip movement along the z -axis. In addition, a bias dc voltage U_{dc} can be optionally superimposed onto the applied voltage between the electrodes without affecting the ac signals.

A. Circuit Analysis of IPBM-SICM

The equivalent circuit of the pipette–sample system in IPBM-SICM is described in our previous work [24] and is illustrated in Fig. 2. The pipette resistance inside the pipette, i.e., R_p , is in series with the resistance of the tip opening region, i.e., R_t , and both of these are in parallel with pipette capacitance C_p . Then, the combined R_p , R_t , and C_p are in series with bath electrolyte resistance R_b . Stray capacitance C_{stray} is in parallel with the above combination. By simultaneously applying an ac voltage U_{ac} at an angular frequency ω ($2\pi f$) coupled with a dc voltage U_{dc} across the two electrodes, the value of the above parameters can be determined by the following measurements, assumptions, and calculations [25].

First, we calculate capacitance C_{stray} by assuming that capacitance C_{stray} remains constant. This assumption is reasonable as the overall external circuit does not change during the experiment. On the basis of this assumption, we can obtain capacitance C_{stray} in advance before the pipette is immersed into the solution [position a, as shown in Fig. 3(a)], where R_p is infinite and C_p is almost zero. In this position, almost all of

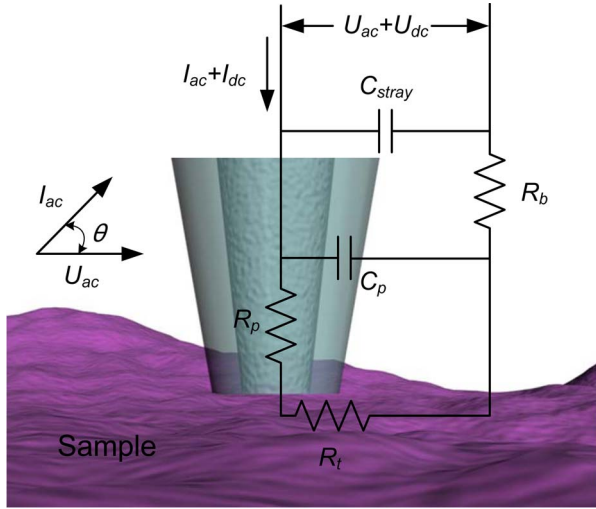


Fig. 2. Circuit analysis of the pipette-sample system in IPBM-SICM.

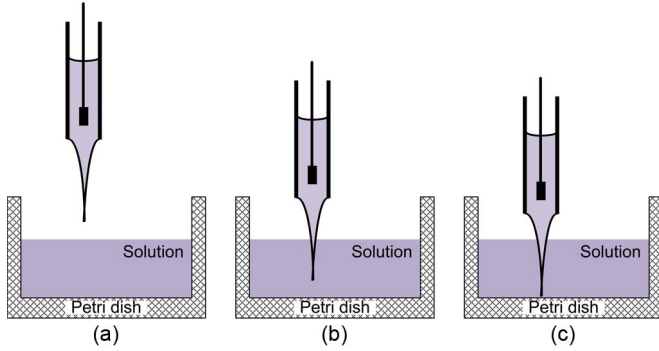


Fig. 3. Analysis of experimental circuit parameters for different positions of the nanopipette. (a) Position a: Tip does not touch the solution. (b) Position b: Tip is immersed several millimeters into the solution but far from the dish. (c) Position c: Tip senses the Petri dish.

the current passes through C_{stray} . Assuming that the total ac current is measured as I_{ac}^* , C_{stray} can be calculated by

$$C_{\text{stray}} = I_{\text{ac}}^* / (U_{\text{ac}} \times \omega). \quad (1)$$

Second, determine R_p and R_t by assuming that R_t is equal to zero when the tip is immersed into the solution but is still far from the sample [position b, as shown in Fig. 3(b)]. At position b [see Fig. 3(b)], we can obtain the amplitude of the ac current I_{ac} , phase θ , and the dc current I_{dc} . I_{ac} and θ are measured from the lock-in amplifier directly, where I_{dc} is calculated by averaging the total current during several tens of modulated periods. According to the dc current path and assuming that $R_{\text{dc}} = R_p + R_t + R_b$ where R_{dc} is the dc resistance, we obtain the following equation:

$$R_p + R_t + R_b = R_{\text{dc}} = U_{\text{dc}} / I_{\text{dc}}. \quad (2)$$

Overall admittance Y can be expressed as

$$Y(j\omega) = A + jB \quad (3)$$

TABLE I
CALCULATED PARAMETERS FOR DIFFERENT POSITIONS IN
FIG. 3 BASED ON THE MODEL IN FIG. 2

	C_{stray} (pF)	C_p (pF)	R_b (M Ω)	R_p (M Ω)	R_t (M Ω)
Position a	3.29	0	unknown	∞	0
Position b	3.29	2.65	0.07	43.6	0
Position c	3.29	3.24	0.07	43.6	28.6

where $A = I_{\text{ac}} \times \cos \theta / U_{\text{ac}}$, and $B = I_{\text{ac}} \times \sin \theta / U_{\text{ac}}$, which can be measured experimentally. The admittance can be also calculated by analyzing the theoretical circuit as follows:

$$Y(j\omega) = \frac{b(1+x^2a)}{1+x^2a^2} + j \left(\frac{bx(1-a)}{1+x^2a^2} + \omega C_{\text{stray}} \right) \quad (4)$$

where $b = 1/R_{\text{dc}}$, $a = bR_b$, and $x = \omega C_p(R_p + R_t)$. By combining (2)–(4) with three available measured quantities, including the amplitude of ac current I_{ac} , the phase of the ac current θ , and the dc current I_{dc} , the unknowns R_b , the combination of R_p and R_t , and C_p can be calculated by

$$R_b = \left(A + \frac{(B')^2}{A-b} \right)^{-1} \quad (5)$$

$$R_p + R_t = \frac{1}{b} - R_b \quad (6)$$

$$C_p = \frac{1}{\omega} \times \frac{1}{R_b} \times \frac{1}{1-bR_b} \times \frac{(A-b)}{B'} \quad (7)$$

where $B' = B - \omega C_{\text{stray}}$. R_t changes with the tip-sample distance, whereas R_p remains constant as it only depends on the geometric shape of the tip. When the tip is far from the sample, R_t can be considered to be zero, and R_p and R_b can be calculated using (5) and (6).

Lastly, when the tip is close to the sample [position c, as shown in Fig. 3(c)], R_t increases as the tip-sample separation decreases. As the known R_p remains constant, the changes of other parameters, including R_t , R_b , and C_p , can be calculated from (5), (6), and (7), respectively. Finally, all of the parameters can be obtained. Table I shows a group of parameters obtained for a specific pipette in one experiment using the aforementioned procedures.

B. Simplified Circuit

In our experiment, R_b is almost negligible as its magnitude is about three orders less than that of R_p , as shown in Table I, which was obtained using a tip with an inner radius of approximately 75 nm. The same conclusion can be also made through experimental results of Unwin group [23]. Therefore, we can neglect R_b to obtain a simplified circuit, as shown in Fig. 4. In the simplified circuit, the total capacitance C_{total} , which includes capacitance C_{stray} and capacitance C_p , is in parallel with the total resistance, which is called the solution resistance R_{sol} . The current through the solution resistance path, i.e., I_{sol} , is in phase with the applied ac voltage and can be obtained by finding the product of I_{ac} and $\cos \theta$, as shown in Fig. 4(b). The in-phase current is inversely related to the

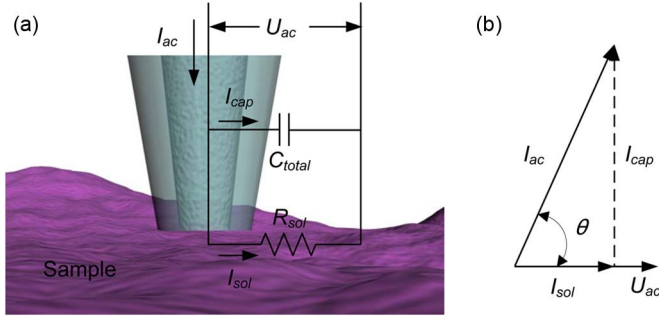


Fig. 4. Simplified circuit of the pipette-sample system in (a) IPBM-SICM and (b) current analysis.

solution resistance R_{sol} and is thus sensitive to the tip-sample separation. As a result, it can be used as a feedback signal to regulate the tip-sample separation. Using the simplified circuit model, dc voltage U_{dc} is not needed for the calibration of all parameters. The unknown parameters R_{sol} and C_{total} in the simplified circuit model can be calculated by

$$R_{sol} = U_{ac} / (I_{ac} \times \cos \theta) \quad (8)$$

$$C_{total} = (I_{ac} \times \sin \theta) / (U_{ac} \times \omega). \quad (9)$$

From (8) and (9), we can determine the solution resistance R_{sol} and capacitance C_{total} from our experimental measurements and hence obtain their dependence on the tip-sample separation, as shown in Fig. 5. Fig. 5(a) indicates that the solution resistance R_{sol} increases but the capacitance C_{total} remains relatively unchanged when the tip-sample separation is reduced. In addition, the zoomed-in data in Fig. 5(b) show that C_{total} slightly increases when the tip is very close to the sample surface, which may be the reason why I_{ac} slightly increases with the decrease in the tip-sample separation, as shown in Fig. 6. This current increase may be also attributed to additional capacitance paths that were formed in the vertical direction of the tip region that accompanied the increase in resistance R_t .

Fig. 6 shows the experimental approach curves that were obtained when the pipette tip approached the Petri dish. These curves show the relationships between different parameters with respect to the tip-sample separation. The total ac current I_{ac} remains relatively constant because it flows mainly through the dominant capacitance path, and it will remain almost constant with relatively constant capacitance. However, the inset in Fig. 6 shows that current I_{ac} slightly increases because of the slightly increased capacitance, as previously discussed. The approach curves of the dc current I_{dc} (see the black line in Fig. 6) and the in-phase ac current I_{sol} (see the red line in Fig. 6) reflect the sensitivity of the control feedback to the tip-sample separation in the dc mode and IPBM mode, respectively. Fig. 6 shows that, as the tip approaches the sample, the sensitivity of the IPBM mode is initially the same as that of the dc mode; however, it becomes less than that of the dc mode as the tip moves closer to the sample surface. This loss in sensitivity may be attributed to the increasing sample capacitance at smaller tip-sample separation [26]. In our experiment, we chose the control setpoint to be 94%–98% of the reference current I_{sol} (recorded far from the sample), and it is located in the overlap-

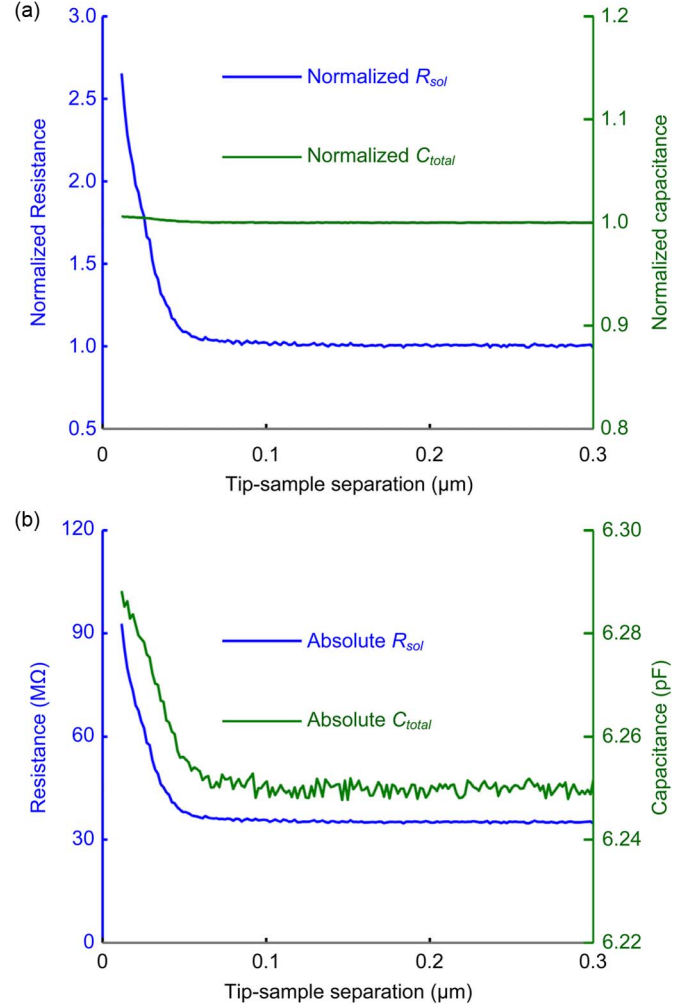


Fig. 5. (a) Normalized and (b) absolute change of calculated solution resistance and capacitance with tip-sample separation in IPBM mode. The modulation frequency is 15 kHz.

ping region of the current I_{sol} and current I_{dc} approach curves. Therefore, the selected setpoint value will provide control performance that is similar to that in the dc mode.

III. CC IN IPBM-SICM

The low-SNR problem in IPBM-SICM is caused by the low signal level of the in-phase current I_{sol} , which is determined by U_{ac} and I_{sol} as

$$I_{sol} = U_{ac} / R_{sol}. \quad (10)$$

When the tip is far away from the sample surface, R_{sol} is constant, and at its minimum value, the reference value of I_{sol} can be obtained using (10). During scanning, I_{sol} is set to 94%–98% of the reference I_{sol} as a control point to regulate the tip movement. However, the magnitude of the reference I_{sol} is limited by the maximum allowable value of the driving U_{ac} , which has to be set to a sufficiently low value to ensure that the total induced ac current I_{ac} is within the input range of the lock-in amplifier (i.e., 1 Vrms in SR830). In the experiment, C_{total} is relatively large and I_{cap} is the dominant contributor

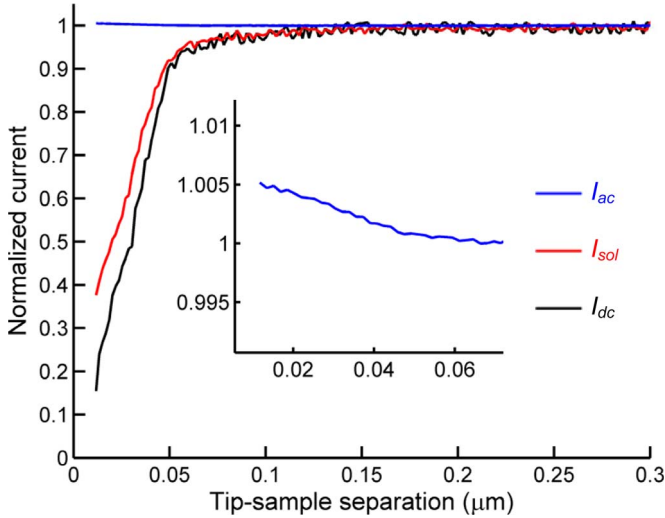


Fig. 6. Approach curves for the relationship between different parameters versus the tip-sample distance in the IPBM mode. As the tip-sample separation reduces, the amplitude of (blue line) the experimental ac current remains almost constant, but the ac current through (red line) the solution resistance path reduces and the change matches well with the right part of (black line) the dc current versus the tip-sample separation. The modulation frequency is 15 kHz.

to the total ac current I_{ac} . Thus, I_{cap} defines the maximum value of U_{ac} to allow I_{ac} to satisfy the input requirement of the lock-in amplifier. For example, using the capacitance and the resistance, as shown in Fig. 5, capacitance C_{total} is 6.2 pF and solution resistance R_{sol} is 35 MΩ. The gain of the I - V converter in the patch clamp amplifier is set to 0.1 mV/pA, and the RMS value of I_{ac} in the SR830 should be less than 10 nA. Therefore, the RMS value of U_{ac} should be less than 17 mV. This low U_{ac} limits the I_{sol} signal to 489 mV after amplifying tenfold through SR830. The half peak-to-peak value of the noise U_{noise} in the experiment is determined by the setting of the lock-in amplifier, usually approximately 10 mV (the lock-in amplifier is set at status II; please refer to Appendix III). Therefore, the noise is greater than 2% of the reference I_{sol} , and the setpoint should be set to much lower than 98%. Moreover, the SNR problem becomes worse at a higher modulation frequency. When f increases to 25 kHz, the reference I_{sol} signal is limited to 293 mV, and in this case, the setpoint should be set to much less than 96.5%.

To solve the problem of low SNR, we introduce the CC method in IPBM-SICM. After incorporating CC, the proportion of I_{cap} in I_{ac} is suppressed, and the driving voltage U_{ac} can therefore be set to a higher value to obtain a larger reference I_{sol} . As shown in Fig. 7(a), there is an additional current path through the extra capacitance C_{comp} and the operational amplifier A_1 . The addition of this extra current I_{comp} is in the opposition direction to I_{cap} and is positively associated with I_{cap} . Their relationship can be derived as

$$I_{comp} = I_{cap} \times (A_1 - 1)C_{comp}/C_{total}. \quad (11)$$

As shown in Fig. 7(b), under a constant U_{ac} , the occurrence of I_{comp} effectively reduces I_{cap} in I_{ac} but does not affect the amount of I_{sol} in I_{ac} . Thus, CC changes I_{ac} into a lower value

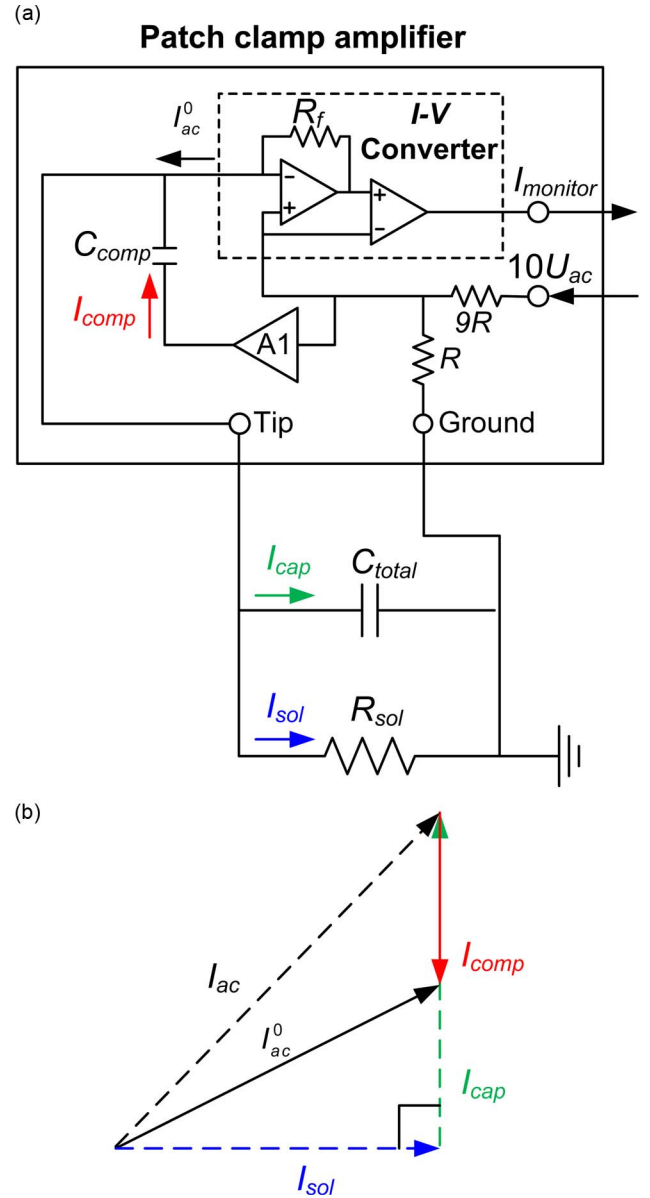


Fig. 7. Schematic IPBM-SICM with CC: (a) circuit model and (b) circuit analysis.

I_{ac}^0 , and it also increases the proportion of I_{sol} in I_{ac} . A larger U_{ac} can therefore be applied before current I_{ac} saturates the input range of the lock-in amplifier. According to (10), I_{sol} is directly proportional to U_{ac} . As a result, the SNR can be improved when the noise level remains unchanged. Equation (11) shows that the degree of compensation can be adjusted by the value of capacitance C_{comp} . A larger CC means that a larger U_{ac} can be set, and hence, a better SNR can be achieved. However, optimal compensation occurs when C_{comp} is equal to $C_{total}/(A_1 - 1)$. Under this optimal compensation, I_{cap} is totally compensated by I_{comp} , and U_{ac} can be set to a maximally allowable value to maximize I_{sol} , thus maximizing the SNR. The improvement in the SNR can be verified by the experimental approach curves at different C_{comp} values, as shown in Fig. 8. Without CC, U_{ac} is limited to 22 mV, causing the noise to be approximately 3% of the reference I_{sol} (see the green line in Fig. 8). When values of

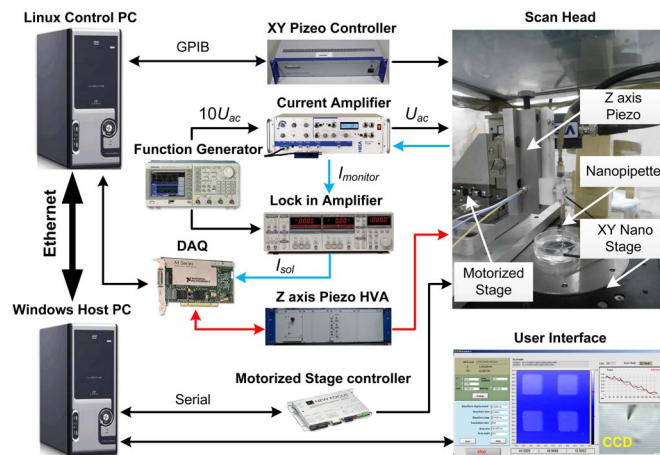


Fig. 9. Configuration of homebuilt IPBM-SICM.

stage (9062-XYZ-PPP, New Focus Corporation, USA) for the large movement of the tip with submicrometer resolution. The control computer, which is equipped with a data acquisition card (PCI-6251, National Instruments, USA), samples the feedback input I_{sol} and the actual displacement of the z -axis piezo, runs the control module, and outputs the control value to regulate the XYZ movement of the tip or sample. The host computer communicates with the control computer via the Internet and provides the interface through which the user can control the scanning procedure or display the topography of the sample. Other key and peripheral devices of the system include an optical microscope, a function generator (Tektronix, AFG3022B), a patch clamp amplifier (Heka, EPC800USB), a lock-in amplifier (Stanford Research Systems, SR830), a piezocontroller, and a motorized stage controller. In addition, the CC circuit is the built-in part of the patch clamp amplifier.

All nanopipettes were fabricated from 1.0-mm-outer-diameter 0.5-mm-inner-diameter borosilicate capillaries (1B100F-4, World Precision Instruments, Shanghai Trading Company Ltd., China) using a CO₂-laser-based pipette puller (P2000, Sutter Instrument, USA), providing tip openings with inner radii of approximately 75 nm and a half cone angle of 4°–5° (confirmed by SEM data, data not shown). In our experiment, the nanopipette was backfilled with a phosphate buffer solution (PBS) and immersed in the PBS solution, and dc resistance R_{dc} was found to be approximately 40–50 MΩ.

In this paper, the ac current I_{ac} was amplified by the I - V converter in the patch clamp amplifier at a gain of 0.1 mV/pA, and cutoff filter frequency is set at 100 kHz. The lock-in amplifier detects the amplitude, phase, and X -out (see Appendix II) of the ac current and outputs the RMS values after they are amplified by a factor of ten times. The values of U_{ac} are set at the maximally allowable value for which I_{sol} does not saturate the lock-in amplifier input.

A. System Setup

B. Sample Preparation

A microgrid made from PDMS was prepared to test the performance of the CC method in IPBM-SICM. The microgrid was fabricated using a soft lithographic approach [27] as follows.

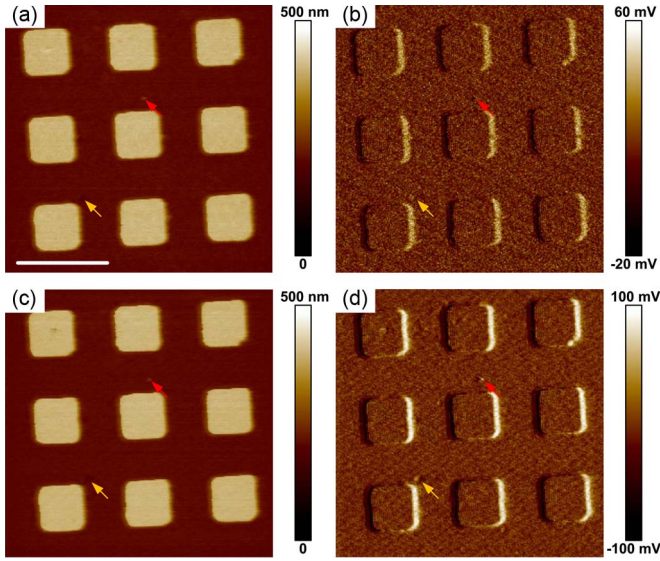


Fig. 10. Comparison of SICM scan images with and without the CC method at the same tip-sample separation (the setpoints are set to 95%). (a) Height image and (b) I_{sol} error image without CC; U_{ac} is set to 22 mV. (c) Height image and (d) I_{sol} error image with 3.5-pF CC; U_{ac} is set to 60 mV. All of the scan images are obtained with a modulation frequency of 15 kHz, Lock in amplifier setting of status III and a scan rate of 0.5 Hz. Bar: 10 μm .

First, a 10 : 1 mixture of PDMS and curing agent (Sylgard 184, Dow Corning) was poured onto a master mold, which is a silicon calibration grating (Digital Instruments, P/N 498-000-026) with a 10- μm pitch and a 200-nm step depth), and it was then baked on a hotplate (PC-600, Corning Inc., USA) at 70 $^{\circ}\text{C}$ for 4 h. Then, PDMS was peeled from the master mold after PDMS had hardened. Finally, a replica of the microgrid in PDMS was obtained with which the surface contacting the master mold was imprinted with the microgrid structure.

C. Applying CC With the Same Tip-Sample Separation as in the Pure IPBM Mode

To investigate how the CC improves the SNR, we first compare the scan results obtained with and without CC by maintaining the same tip-sample separation during scanning. As shown in Fig. 10, when applying CC or not, the height images seem similar; however, the error images seem different. In error images, fine structures pointed by the arrows can be only distinguished from the background noise with CC, which is due to the improved SNR. Without CC, U_{ac} is limited to 22 mV and the error signal of fine structures is covered by the noise, as shown in Fig. 10(b). On the contrary, the expanding signal will stand out from the same noise level after CC when U_{ac} is set to 60 mV, as shown in Fig. 10(d). Therefore, the quality of the error image in the IPBM mode is improved with the CC method because of the improved SNR.

D. Applying CC With Larger Tip-Sample Separation

With the CC method, a larger tip-sample separation (higher setpoint) can be applied during scanning. Without compensa-

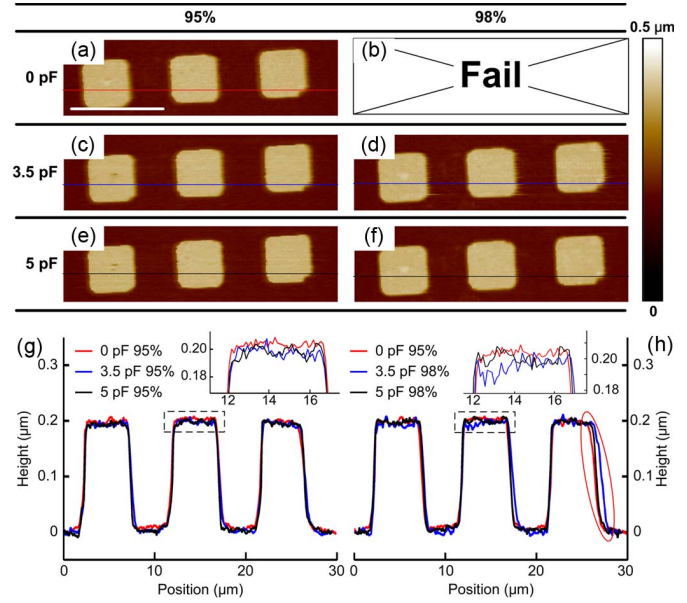


Fig. 11. Comparison of SICM scan images with and without the CC method at different tip-sample separations. (a) Height image without CC when setpoint is 95% and U_{ac} is set to 22 mV. (b) We failed to obtain the image without CC when setpoint is 95% and U_{ac} is set to 22 mV. (c) and (d) Height images with 3.5-pF CC and 60-mV U_{ac} , whereas (c) and (d) are obtained at 95% and 98% tip-sample separation, respectively. (e) and (f) Height images with 5-pF CC and 160-mV U_{ac} , whereas (e) and (f) are obtained at 95% and 98% tip-sample separation, respectively. Lower panel (g) shows line profiles from the red line in (a), the blue line in (c), and the black line in e. The inset is a zoom-in of the height profiles in (g). (h) Contrast of line profiles from the red line in (a), the blue line in (d), and the black line in (f). The inset is a zoom-in of the height profiles in (h). All of the scan images are obtained with a modulation frequency of 15 kHz, lock-in amplifier setting of status III, and a scan rate of 0.5 Hz. Bar: 10 μm .

tion, the setpoint should be set to lower than 98% because of the low SNR (see the green line in Fig. 8). When values of 3.5 or 5 pF are compensated, the setpoint can be set to be 98% with an increased value of U_{ac} . Moreover, the experimental results show that images obtained with enough CC, which allow a large tip-sample separation [see Fig. 11(f)], have similar quality to those obtained without CC, which requires a small tip-sample separation [see Fig. 11(a)]. However, as shown in the red circle in Fig. 11(h), at larger tip-sample separation with smaller CC, i.e., 3.5 pF, parachuting (image blurring in the downhill region of grating) issue occurs sometimes due to the relatively low SNR (see the red line in Fig. 8). In addition, a larger tip-sample separation reduces the sample distortion during scanning. During practical operation, the electrolyte filling level is always different from the equilibrium value that is determined by the capillary tension, which leads to a hydrostatic force that is inversely proportional to the tip-sample separation [28]. In this case, the sample suffers from a larger hydrostatic force as the tip-sample separation is reduced, thus causing a larger sample distortion.

E. Applying CC at Larger Modulation Frequency

With the CC method, a larger modulation frequency can be applied during scanning. When the modulation frequency is set

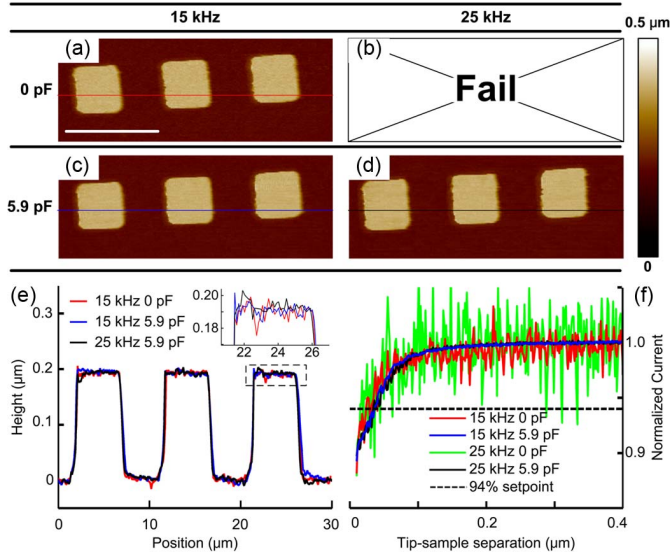


Fig. 12. Comparison of SICM results with and without the CC method at different modulation frequencies. (a) Height image without CC when the modulation frequency is 15 kHz and U_{ac} is set to 20 mV. (b) We failed to obtain the image without CC when the modulation frequency is 25 kHz and U_{ac} is maximized to be 9.5 mV. (c) Height image with 5.9-pF CC when the modulation frequency is 15 kHz and U_{ac} is set to 180 mV. (d) Height image with 5.9-pF CC when the modulation frequency is 25 kHz and U_{ac} is set to 100 mV. (e) Contrast of the line profiles from the red line in (a), the blue line in (c), and the black line in (d). The inset is a zoom-in of the height profiles in (e). (f) Experimental approach curves with and without the CC method at different modulation frequencies. All of the scan images are obtained when the lock-in amplifier is set at status II, the scan rate is 0.5 Hz, and the setpoints are set to 94%. Bar: 10 μm .

to 15 kHz, without CC U_{ac} is limited to 20 mV, we can obtain the image at 94% setpoint, although the SNR [see the red line in Fig. 12(f)] is very low. If f increases to 25 kHz, I_{ac} will increase and U_{ac} has to be reduced to a lower value (limited to 9.5 mV). This will further reduce I_{sol} , and thus, the noise to reference I_{sol} becomes larger [see the green line in Fig. 12(f)]. Such a low SNR is unacceptable for imaging. However, after applying CC with a larger U_{ac} , the SNR can be significantly improved [see the blue line in Fig. 12(f)], and it can be also improved at a larger modulation frequency of 25 kHz [see the black line in Fig. 12(f)]. Therefore, with the improved SNR after CC, SICM can function at a larger modulation frequency, i.e., 25 kHz. Moreover, the line profiles show that the images' quality with CC [see Fig. 12(c) and (d)] seems similar with the one obtained without CC [see Fig. 12(a)]. However, the low-SNR problem can be also inferred from the error images, and the one without CC (data not shown) is more blurring.

F. Applying CC at Higher Scan Speed

With the CC method, a larger scan speed can be used during scanning. Without CC, when the modulation frequency is set to 15 kHz and the setpoint is set to 94%, U_{ac} is limited to 20 mV, and hence, the SNR limits the lock-in amplifier to set at status II. Such induced low bandwidth of the lock-in amplifier makes the gain parameters of PID control larger enough to avoid parachuting or to shorten the parachuting period [29]. However,

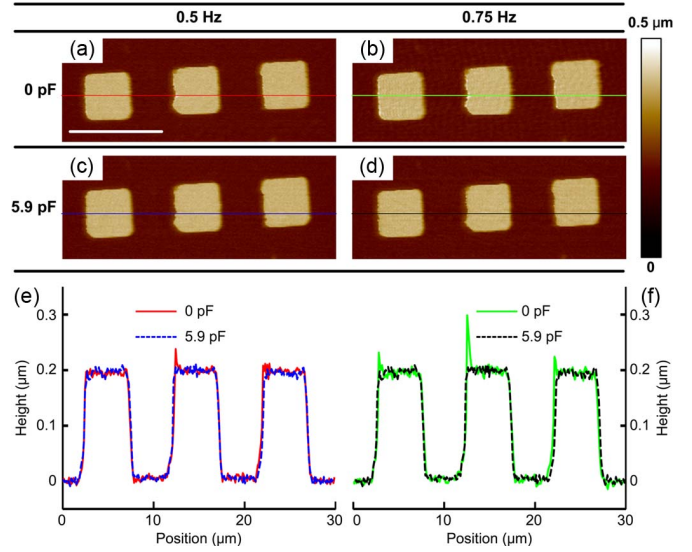


Fig. 13. Comparison of SICM results with and without the CC method at different speeds. (a) and (b) Height images without CC when U_{ac} is set to 20 mV, and the lock-in amplifier is set at status II. The difference is the scan rate of (a) is 0.5 Hz, and the one of (b) is 0.75 Hz. (c) and (d) are height images with 5.9 pF CC when U_{ac} is set to 180 mV, the lock-in amplifier is set at status IV. And the difference is the scan rate of c is 0.5 Hz and the one of d is 0.75 Hz. (e) Contrast of the line profiles from the red line in (a) and the blue line in (c). (f) Contrast of the line profiles from the green line in b and the black line in d. The entire scan images are obtained under the following conditions: The modulation frequency is 15 kHz, and the setpoints are set to 94%. Bar: 10 μm .

with large gain parameter, tip will be easy to overshoot [see the red line in Fig. 13(e)] at the uphill of grating when scan rate is 0.5 Hz, as shown in Fig. 13(a). It becomes worse when the scan speed increases to 0.75 Hz, as shown in Fig. 13(b). CC method improves the SNR problem and lets the lock-in amplifier work at status IV, expanding the bandwidth of the lock-in amplifier (please refer to Appendix III). With the expanding bandwidth, no overshoot is found in the image [see Fig. 13(c)] even the one with a faster scan rate at 0.75 Hz [see Fig. 13(d)]. Therefore, with the improved SNR after CC, SICM can function at a larger scan rate frequency, i.e., 0.75 Hz. In addition, our current speed is limited by the bandwidth of the piezoactuator. When at the increasing further scan rate, i.e., 1 Hz, oscillating problem will start to occur (data not shown), and it would not help with a higher modulated frequency.

V. CONCLUSION

In summary, we have developed a CC method to solve the low-SNR problem in IPBM-SICM, and the effectiveness of the proposed CC method was shown by performing imaging on PDMS samples at different tip-sample separations and different modulation frequencies. The CC method not only allows the IPBM-SICM to work at larger tip-sample separations but also be capable to work at larger modulation frequencies. These improvements will reduce the tip-sample force and improve the scan speed in IPBM-SICM. Thus, it will provide further opportunities for fast imaging of living cells in our future work.

APPENDIX I

MODULATION FREQUENCY VERSUS SCANNING SPEED

Similar to the theoretical consideration of the maximum scan speed in the tapping mode AFM proposed by the Ando group [30], [31], in IPBM-SICM, we can derive the relationship between the scanning speed and the modulation frequency f . Assuming that the sample has a sinusoidal shape with periodicity λ , for an $N \times N$ -pixel image, the smallest imaging acquisition time T of SICM can be expressed as

$$T > 16npN^2/(\lambda f) \quad (12)$$

where n is the minimum number of waves for the RMS of current I_{sol} and p is the pixel size. Therefore, the smallest imaging acquisition time is limited by the modulation frequency f . This relationship between the imaging time and the modulation frequency also applies in the traditional ac mode SICM. In our system, a higher modulation frequency (greater than 25 kHz) is realized, which is much higher than that in the traditional ac mode (limited to be 1 kHz to several kilohertz), and is expected to help accelerate the scan speed.

APPENDIX II

X-OUTPUT OF THE LOCK-IN AMPLIFIER

Dual-phase lock-in amplifiers such as SR830 have two phase-sensitive detectors (PSDs): One multiplies the input signal by the reference signal (provided by either the internal oscillator or an external source), whereas the other multiplies the signal with the reference signal shifted by 90° .

Assuming that the input signal and reference signal are $V_{sig} \sin(\omega_{sig}t + \theta_{sig})$ and $V_{ref} \sin(\omega_{ref}t + \theta_{ref})$, respectively, the product of the first PSD is

$$\begin{aligned} V_{psd1} &= V_{sig} \sin(\omega_{sig}t + \theta_{sig}) \cdot V_{ref} \sin(\omega_{ref}t + \theta_{ref}) \\ &= 1/2 V_{sig} V_{ref} \cos[(\omega_{sig} - \omega_{ref})t + (\theta_{sig} - \theta_{ref})] \\ &\quad - 1/2 V_{sig} V_{ref} \cos[(\omega_{sig} + \omega_{ref})t + (\theta_{sig} + \theta_{ref})] \end{aligned} \quad (13)$$

where the first part of the PSD output is at the difference frequency $(\omega_{sig} - \omega_{ref})$, and the latter is at the sum frequency $(\omega_{sig} + \omega_{ref})$. After the PSD output passes through a low-pass filter, the ac component will be removed. In addition, if ω_{sig} is not equal to ω_{ref} , then the two parts are ac signals and nothing will remain; otherwise, the component at the difference frequency will be a dc signal and will remain. In this case, the first filtered PSD output V_{psd1} will be

$$V_{psd1} = 1/2 V_{sig} V_{ref} \cos(\theta_{sig} - \theta_{ref}). \quad (14)$$

Setting $X = V_{sig} \cos \theta$ and letting θ be the phase difference between the signal and reference, and using (14), X can be calculated by dividing V_{psd1} by a known parameter $1/2 V_{ref}$. X is also called the “in-phase” component because, when the difference phase is zero, X then measures the signal. Similarly, the filtered output of the second PSD V_{psd2} gives the out-of-phase component Y (equal to $V_{sig} \sin \theta$). Then, using both X

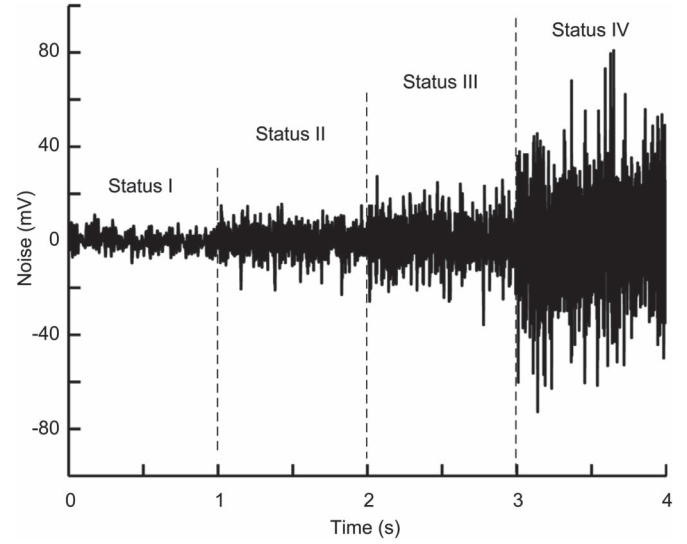


Fig. 14. Relationship between noise and bandwidth in lock-in amplifier SR830. The noise is recorded when the time constant is setting at different values, for example, status I (T_{const} 1 ms), status II (T_{const} 300 μ s), status III (T_{const} 100 μ s), and status IV (T_{const} 30 μ s). The modulated frequency is set at 25 kHz, and the slope is set at 24 dB/oct.

and Y , amplitude V_{sig} and the difference phase θ of the input signal can be calculated.

In SR830, X can be outputted after being amplified tenfold, and the output is called the 10X output. In addition, both X and Y are continuous signals and therefore have a larger bandwidth than amplitude V_{sig} and phase θ , which are discrete signals.

APPENDIX III

BANDWIDTH AND NOISE OF THE LOCK-IN AMPLIFIER

In SR830, the bandwidth is given by the effective noise bandwidth, and specified in the manual (pages 3–11). ENBW is determined by the time constant T_{const} and slope setting, and a simplified calculated formula is also concluded in the manual (pages 3–21). When the slope setting is constant at 24 dB/oct, the relationship between ENBW and T_{const} is

$$ENBW = 5/(64T_{const}). \quad (15)$$

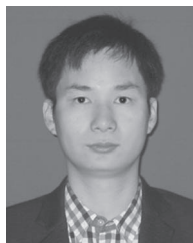
From (15), we can conclude that ENBW has negative correlation with T_{const} . Hence, when T_{const} is reducing, the bandwidth will be expanded. However, this comes at the price of an increasing noise. (Please see the simplified formula of Johnson noise in pages 3–21 of the manual.)

In summary, when the time constant is set smaller, the bandwidth will be larger, but the current noise is increasing as well. This relationship will be verified by the experimental result, as shown in Fig. 14.

REFERENCES

- [1] P. K. Hansma, B. Drake, O. Marti, S. A. C. Gould, and C. B. Prater, “The scanning ion-conductance microscope,” *Science*, vol. 243, no. 4891, pp. 641–643, Feb. 1989.
- [2] S. Zhang *et al.*, “Scanning ion conductance microscopy studies of amyloid fibrils at nanoscale,” *Nanoscale*, vol. 4, no. 10, pp. 3105–10, May 2012.

- [3] P. Happel, D. Thatenhorst, and I. D. Dietzel, "Scanning ion conductance microscopy for studying biological samples," *Sensors*, vol. 12, no. 11, pp. 14983–15008, Nov. 2012.
- [4] P. Novak *et al.*, "Nanoscale live-cell imaging using hopping probe ion conductance microscopy," *Nature Methods*, vol. 6, no. 4, pp. 279–281, Mar. 2009.
- [5] R. A. Seger *et al.*, "Voltage controlled nano-injection system for single-cell surgery," *Nanoscale*, vol. 4, no. 19, pp. 5843–5846, Sep. 2012.
- [6] P. Actis *et al.*, "Compartmental genomics in living cells revealed by single-cell nanobiopsy," *ACS Nano*, vol. 8, no. 1, pp. 546–553, Nov. 2013.
- [7] D. Sanchez *et al.*, "Localized and non-contact mechanical stimulation of dorsal root ganglion sensory neurons using scanning ion conductance microscopy," *J. Neurosci. Methods*, vol. 159, no. 1, pp. 26–34, Jan. 2007.
- [8] J. Gorelik *et al.*, "Ion channels in small cells and subcellular structures can be studied with a smart patch-clamp system," *Biophys. J.*, vol. 83, no. 6, pp. 3296–3303, Dec. 2002.
- [9] Y. Takahashi *et al.*, "Simultaneous noncontact topography and electrochemical imaging by SECM/SICM featuring ion current feedback regulation," *J. Amer. Chem. Soc.*, vol. 132, no. 29, pp. 10118–10126, Jun. 2010.
- [10] Y. Takahashi *et al.*, "Multifunctional nanoprobe for nanoscale chemical imaging and localized chemical delivery at surfaces and interfaces," *Angew. Chem. Int. Ed.*, vol. 50, no. 41, pp. 9638–9642, Sep. 2011.
- [11] S. C. Lai, P. V. Dudin, J. V. Macpherson, and P. R. Unwin, "Visualizing zeptomole (electro)catalysis at single nanoparticles within an ensemble," *J. Amer. Chem. Soc.*, vol. 133, no. 28, pp. 10744–10747, Jul. 2011.
- [12] A. Bruckbauer, L. M. Ying, A. M. Rothery, Y. E. Korchev, and D. Klennerman, "Characterization of a novel light source for simultaneous optical and scanning ion conductance microscopy," *Anal. Chem.*, vol. 74, no. 11, pp. 2612–2616, Apr. 2002.
- [13] Y. E. Korchev, C. L. Bashford, M. Milovanovic, I. Vodyanoy, and M. J. Lab, "Scanning ion conductance microscopy of living cells," *Biophys. J.*, vol. 73, no. 2, pp. 653–658, Aug. 1997.
- [14] A. I. Shevchuk *et al.*, "Simultaneous measurement of Ca²⁺ and cellular dynamics: Combined scanning ion conductance and optical microscopy to study contracting cardiac myocytes," *Biophys. J.*, vol. 81, no. 3, pp. 1759–1764, Sep. 2001.
- [15] D. Pastre, H. Iwamoto, J. Liu, G. Szabo, and Z. F. Shao, "Characterization of AC mode scanning ion-conductance microscopy," *Ultramicroscopy*, vol. 90, no. 1, pp. 13–19, Nov. 2001.
- [16] C. A. J. Putman, K. O. Vanderwerf, B. G. Degrooth, N. F. Vanhulst, and J. Greve, "Tapping mode atomic-force microscopy in liquid," *Appl. Phys. Lett.*, vol. 64, no. 18, pp. 2454–2456, May 1994.
- [17] J. W. Wu, K. C. Huang, M. L. Chiang, M. Y. Chen, and L. C. Fu, "Modeling and controller design of a precision hybrid scanner for application in large measurement-range atomic force microscopy," *IEEE Trans. Ind. Electron.*, vol. 61, no. 7, pp. 3704–3712, Jul. 2014.
- [18] C. Li *et al.*, "High resolution imaging using scanning ion conductance microscopy with improved distance feedback control," *Progr. Nat. Sci.*, vol. 18, no. 6, pp. 671–677, Jun. 2008.
- [19] Y. Takahashi *et al.*, "Topographic imaging of convoluted surface of live cells by scanning ion conductance microscopy in a standing approach mode," *Phys. Chem. Chem. Phys.*, vol. 12, no. 34, pp. 10012–10017, Sep. 2010.
- [20] S. A. Mann, G. Hoffmann, A. Hengstenberg, W. Schuhmann, and I. D. Dietzel, "Pulse-mode scanning ion conductance microscopy - a method to investigate cultured hippocampal cells," *J. Neurosci. Methods*, vol. 116, no. 2, pp. 113–117, May 2002.
- [21] P. Happel, G. Hoffmann, S. A. Mann, and I. D. Dietzel, "Monitoring cell movements and volume changes with pulse-mode scanning ion conductance microscopy," *J. Microsci.*, vol. 212, pp. 144–151, Nov. 2003.
- [22] P. Happel and I. D. Dietzel, "Backstep scanning ion conductance microscopy as a tool for long term investigation of single living cells," *J. Nanobiotechnol.*, vol. 7, pp. 7, Oct. 2009.
- [23] K. McKelvey, D. Perry, J. C. Byers, A. W. Colburn, and P. R. Unwin, "Bias modulated scanning ion conductance microscopy," *Anal. Chem.*, vol. 86, no. 7, pp. 3639–3646, Apr. 2014.
- [24] P. Li *et al.*, "Phase modulation mode of scanning ion conductance microscopy," *Appl. Phys. Lett.*, vol. 105, no. 5, Aug. 2014.
- [25] M. Lindau and E. Neher, "Patch-clamp techniques for time-resolved capacitance measurements in single cells," *Pflugers Arch.*, vol. 411, no. 2, pp. 137–146, Feb. 1988.
- [26] K. McKelvey, S. L. Kinnear, D. Perry, D. Momotenko, and P. R. Unwin, "Surface charge mapping with a nanopipette," *J. Amer. Chem. Soc.*, vol. 136, no. 39, pp. 13735–13744, Oct. 2014.
- [27] Y. N. Xia and G. M. Whitesides, "Soft lithography," *Annu. Rev. Mater. Sci.*, vol. 28, no. 1, pp. 153–184, Aug. 1998.
- [28] M. Pellegrino *et al.*, "Weak hydrostatic forces in far-scanning ion conductance microscopy used to guide neuronal growth cones," *Neurosci. Res.*, vol. 69, no. 3, pp. 234–240, Mar. 2011.
- [29] N. Kodera, M. Sakashita, and T. Ando, "Dynamic proportional-integral-differential controller for high-speed atomic force microscopy," *Rev. Sci. Instrum.*, vol. 77, no. 8, Aug. 2006, Art. ID. 083704.
- [30] T. Ando, T. Uchihashi, and T. Fukuma, "High-speed atomic force microscopy for nano-visualization of dynamic biomolecular processes," *Progr. Surf. Sci.*, vol. 83, no. 7–9, pp. 337–437, Nov. 2008.
- [31] T. Ando, T. Uchihashi, and N. Kodera, "High-speed AFM and applications to biomolecular systems," *Annu. Rev. Biophys.*, vol. 42, pp. 393–414, 2013.



nanosystems.

Peng Li (S'12) received the B.S. degree in automation from Sichuan University, Chengdu, China, in 2009. He is currently working toward the Ph.D. degree in mechanical and electrical engineering at Shenyang Institute of Automation, Chinese Academy of Sciences, Shenyang, China.

He is also with the University of the Chinese Academy of Sciences, Beijing, China. His current research interests include single-cell analysis technique, circuit analysis, and micro/



biosensors.

Lianqing Liu (M'09) received the B.S. degree in industry automation from Zhengzhou University, Zhengzhou, China, in 2002 and the Ph.D. degree from the Chinese Academy of Sciences, Shenyang, China, in 2009.

He is currently a Professor with Shenyang Institute of Automation, Chinese Academy of Sciences. His current research interests include nanorobotics, intelligent control, and biosensors.

Prof. Liu was a recipient of the Early Government/Industrial Career Award by the IEEE Robotics and Automation Society in May 2011, the Lu Jiaxi Young Scientist Award of the Chinese Academy of Sciences in January 2011, and the President Award of the Chinese Academy of Sciences in 2009.



Yang Yang received the B.S. degree in measurement and control technology and instrumentation and the M.S. degree in mechanical and electronic engineering from Dalian University of Technology, Dalian, China, in 2004 and 2008, respectively.

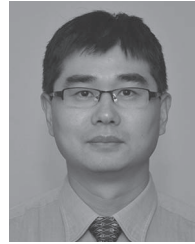
He is currently an Associate Professor with Shenyang Institute of Automation, Chinese Academy of Sciences, Shenyang, China. His current research interests include micro/nanosystems, circuit design and analysis, and



nanomanipulations.

Yuechao Wang (M'12) received the M.S. degree in pattern recognition and intelligent control from the Chinese Academy of Sciences, Shenyang, China, in 1987 and the Ph.D. degree in mechatronic engineering from Harbin Institute of Technology, Harbin, China, in 1999.

Since 1987, he has been with Shenyang Institute of Automation, Chinese Academy of Sciences, where he is currently a Professor. His current research interests include robot control, multirobot systems, and micro/



Guangyong Li (M'07) received the B.S. degree in mechanical engineering from Nanjing University of Aeronautics and Astronautics, Nanjing, China, in 1992, the M.S. degree in aerospace engineering from Beijing Institute of Control Engineering, China Academy of Space Technology, Beijing, China, in 1999, and the Ph.D. degree in electrical engineering from Michigan State University, East Lansing, MI, USA, in 2006.

He is currently an Associate Professor with the Department of Electrical and Computer Engineering, University of Pittsburgh, Pittsburgh, PA, USA. His current research interests include micro/nanorobotic systems; fabrication of microelectromechanical systems/nanoelectromechanical systems, nanodevices, and biosensors; control theory and applications, real-time system design, implementation, and integration; and neural network control.

Dr. Li and his coauthors were the recipient of the 2006 IEEE TRANSACTIONS ON AUTOMATION SCIENCE AND ENGINEERING Best Paper Award.